PHYSICAL REVIEW E **105**, 034702 (2022)

Wrinkling pattern formation with periodic nematic orientation: From egg cartons to corrugated surfaces

Ziheng Wang,[*] Phillip Servio,[†] and Alejandro Rey[‡]
Department of Chemical Engineering, McGill University, 3610 University Street, Montréal, Québec, Canada H3A 0C5

(Received 24 November 2021; accepted 4 March 2022; published 23 March 2022)

Egg cartons, known as doubly sinusoidal surfaces, display a rich variety of saddles-cylinder-spherical patches organized with different spatial symmetries and connectivities. Egg carton surfaces, rich in functionalities, are observed in synthetic and biological materials, as well as across atomic and macroscopic scales. In this work we use the liquid crystal shape equation in the absence of elastic effects and normal stress jumps to predict and classify a family of uniaxial, equibiaxial, and biaxial egg cartons, according to the periodicities of the surface director field in nematic (N) and cholesteric (N*) liquid crystals under the presence of anisotropic surface tension (anchoring). Egg carton surface shape periodic solutions to the nonlinear and linearized liquid crystal shape equations predict that the mean curvature is a linear function of the orthogonal (along the surface normal) splay and bend contributions. Mixtures of egg carton surfaces (uniaxial, equibiaxial, and biaxial) emerge according to the symmetries of the nonsingular director field, and the spatial distributions of the director escape into the third dimension; pure uniaxial egg cartons emerge when the director escape has linelike geometries and mixtures of egg cartons arise under source or sink orientation lattices. Orientation symmetry and permutation analysis are incorporated into a full curvature (Casorati, shape parameter, mean curvature, and Gaussian curvature) characterization. Under a fixed anchoring parameter, conditions for maximal nanoscale curvedness and microscale maximal shape gradient diversity are identified. The present results contribute to various pathways to surface pattern formation using intrinsic anisotropic interfacial tension.

DOI: 10.1103/PhysRevE.105.034702

I. INTRODUCTION

Nematic (N) and chiral nematic (N* or cholesteric CLC) liquid crystals are anisotropic viscoelastic soft matter multifunctional materials. Surface and bulk functionalities are ubiquitous in nature's fibrous composites known as liquid crystal analogs, where the liquid crystal orientational order is frozen-in in the solid state. Biological cholesteric liquid crystal analogs displaying the Bouligand plywood architecture include chitins in the beetle's exoskeleton [1,2], cellulose in tulips [3–5], rose petals [6], collagen in human compact bone [7], and many others [8–10]. The Bouligand's twisted plywood structure [11–13] is responsible for multifunctionalities such as iridescence in scarab beetles [14] and stress wave filtering within the dactyl club of the stomatopod [15]. Surface functionalities in liquid crystal analogs, such as tribological, and wetting, are closely associated with surface wrinkling patterns [16]. Biological wrinkling patterns serve as biomimetic inspiration for other metallic materials [17]. Besides submicron and micron wrinkling, geological structures also display geometrically similar wrinkling at large macroscopic scales, but due to different processes [18]. Hence wrinkling-based pattern formation offers pathways to embed functionalities to soft and hard materials and characterize the geometry of biological and geological structures across length scales. This paper focuses only on wrinkling patterns in N and N* surfaces. To establish the scope of the paper and introduce the main focus and objectives of this work we briefly describe the geometric classification of common wrinkling patterns in terms of dimensionality and then describe driving forces behind these patterns.

There are three primitive wrinkling modes that will be considered in this paper, according to the spatial functionality of the surface height function $h(x, y)$; here we use the Monge surface parametrization $[x, y, h(x, y)]$ [19].

(i) Uniaxial wrinkling h_{uni}: the surface shows a periodic wrinkling pattern along one spatial direction and remains flat on the other direction (vanishing Gaussian curvature). This is a corrugated surface; it has zero Gaussian curvature and is composed of cylindrical patches. This wrinkling group encloses the morphology of tulip *Queen of the Night* [20]. Uniaxial wrinkling is only depending on one spatial coordinate, where $h_{\mathrm{uni}} = f(x)$ or $h_{\mathrm{uni}} = f(y)$.

(ii) Equibiaxial wrinkling h_{eq}: this type of surface exhibits regular sinusoidal patterns along both spatial coordinates, which are sometimes also called concave or convex [21], sinusoidal [22], or ideal equibiaxial egg carton surface [23]. For an equibiaxial doubly periodic wrinkling surface, the spatial coordinates play a symmetric role such that $h_{\mathrm{eq}}(x, y) = h_{\mathrm{eq}}(y, x)$.

(iii) Biaxial wrinkling $h_{\mathrm{bi}}(x, y)$: the two spatial coordinates do not play a symmetric role. This pattern is denoted as biaxial egg carton. This mode includes electropolished metal surfaces [17] and erosion-driven rocks [18]. The periodicity

---

[*] ziheng.wang@mail.mcgill.ca

[†] phillip.servio@mcgill.ca; https://hydratetech.com/

[‡] alejandro.rey@mcgill.ca; http://mmrg.chemeng.mcgill.ca/

along the x coordinate is different than the periodicity along the y coordinate.

We expect a regular wrinkling surface $h(x, y)$ can be decomposed as a linear combination of the three modes mentioned above $h(x, y) = a_1 h_{\mathrm{uni}} + a_2 h_{\mathrm{eq}} + a_3 h_{\mathrm{bi}}$, which is a result that we prove below.

Next we briefly discuss connections between the wrinkling geometry and driving forces acting on a N or N* surface, defined by its geometry (unit normal $\mathbf{k}$ and curvature tensor $\mathbf{B}$) and structure (director $\mathbf{n}$ and its surface gradient $\nabla_{(\sigma)}\mathbf{n}$) [24]. Given the dual characteristics of these surfaces, in the absence of convection, characterizing an N or N* surface requires satisfying the bulk and surface torque balance equations for $\mathbf{n}$ and a scalar shape equation [25]. According to the generalized liquid crystal shape equation, the various terms include the bulk elastic normal stress jump, the Laplace pressure, the Herrings (surface rotation) pressure, and the director pressure from its surface gradients [24,26]. Hence the source of potential surface pattern formation mechanisms in nematics is extremely rich and varied even for a single component material.

In the absence of the bulk elastic normal stress jump, nematic surface pattern formation is the balance of all three above-mentioned pressures or, equivalently, the vanishing of the total capillary pressure. The condition of zero capillary pressure corresponds to a special shape known as easy shape [25,27], which involves couplings between geometric and structural variables and contrary to isotropic material surfaces does not need to be a flat surface or a minimal surface. The couplings involve the anchoring coefficient which introduces the anisotropic interfacial energy component into the interfacial energy. Given these facts, we expect that doubly periodic director orientation fields will coexist with periodic wrinkling surface patterns and determine the nature and magnitude of the coefficients $\{a_i,\ \ i = 1, 2, 3\}$ introducing the primitive modes in the generalized wrinkling surface $h(x, y)$ discussed above. Both nematic N and cholesteric N* liquid crystal can exhibit complex two-dimensional (2D) director fields, either due to external fields (flow [28,29] and electromagnetics [30]), phase transition or separation [31–33], and more [34–36]. Hence exploring these orientation landscapes of soft matter materials in the context of surface pattern formation such as wrinkling is a potentially fruitful addition to other routes using high temperature–metal based systems as well as providing insights into natures' patterns.

Uniaxial surface wrinkling h_{uni} (cylinders with zero Gaussian curvature) has been previously discussed with a simple quadratic [37–42] or quartic [43] anisotropic surface tension, where the energy is minimized by the fact that surface unit normal $\mathbf{k}$ tends to adjust its relative angle with respect to the director field $\mathbf{n}$. We also found that complex surface cylindrical surface patterns can be obtained by including higher-order terms in the Rapini-Papoular equation.

Biaxial wrinkling h_{bi} has been successfully modeled by elastic theory [44] and mean-field theory [45]. Anchoring-driven biaxial wrinkling was briefly studied by generalizing and linearizing the uniaxial wrinkling model in [46], using a driven wave-propagation method and sequential wrinkling. However, for spontaneous self-selected pattern formation the wave-propagation mechanism is incomplete since the rotation effect is neglected. Here we formulate and solve an integrated model using both global (physical coordinates) and local (surface coordinates) perspectives, consistent with experimental results [16,47–49].

Figure 1 summarizes the scope and objectives of this paper that includes both cholesteric N* and nematic N liquid crystals' free surfaces in the total absence of bulk elastic effects. For a given distorted director nonplanar director field (b), capillary pressure will create surface wrinkling patterns (b) according to the specific symmetry of director splay and bend deformations' modes. The surface modes include uniaxial, equibiaxial, and biaxial wrinkling and the corresponding wavelengths' magnitudes are indicated by P_0. The key objective of this work is to establish the connection and dependence of the egg carton surface pattern formation process on the director $\mathbf{n}$ deformation modes of cholesteric and achiral nematic liquid crystals.

The outline of this paper is as follows. The general methodology is introduced in Sec. II. The physical background of liquid crystals is given in Sec. II A [surface and bulk properties in Fig. 1(a)]. The general frameworks on director field and geometry are given in Sec. II B [Fig. 1(a)]

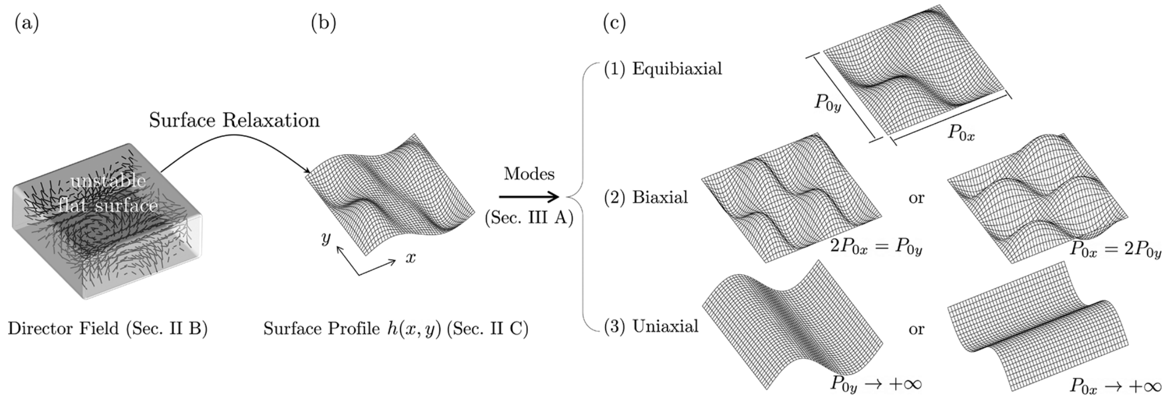

FIG. 1. Distorted chiral nematic liquid crystals generally do not have a stable flat surface (a); the capillary pressures [in Eq. (7)] drive the surface relaxation process to a corrugated pattern (b), which can be decomposed by three primitive egg carton modes: equibiaxial, biaxial, and uniaxial wrinkling (c). Here P_0 denotes the scale of the pattern.

and Sec. II C, respectively. Combining the two frameworks we are able to formulate the governing equation in Sec. II D [driving forces from Fig. 1(a) to Fig. 1(b)], with a full director model (Sec. II D 1), a decomposition model (Sec. II D 2), and a linear approximation model (Sec. II D 3). The highly accurate and validated numerical methods are introduced in Sec. II E. The results are evaluated in Sec. III [Fig. 1(b)], which includes surface reliefs (Sec. III A) and curvature profiles (Sec. III B). The important conclusions and significance are summarized in Sec. IV. The Appendixes provide details of all mathematical derivations and numerical techniques.

II. METHODOLOGY

A. Interfacial energy and bulk deformation modes

The surface energy density can be described by the second order Rapini-Papoular equation [50,51]

$$\gamma = \gamma_0 + \frac{W}{2}\mathbf{nn} : \mathbf{kk}, \tag{1}$$

where γ_0 is the isotropic surface tension and W is the anchoring coefficient. We denote the dimensionless anchoring coefficient as $\epsilon = W/\gamma_0$, restricted to $\epsilon > -2$.

In the Oseen-Frank elastic theory [51,52], three independent elastic modes are defined by

$$\mathbb{S} = \nabla \cdot \mathbf{n}, \quad \mathbb{T} = \mathbf{n} \cdot \nabla \times \mathbf{n}, \quad \mathbb{B} = \mathbf{n} \times \nabla \times \mathbf{n}, \tag{2}$$

which capture splay, twist, and bending distortions of the director field $\mathbf{n}$, respectively.

B. Director field general framework

In this paper, the surface director field $\mathbf{n}$ is known and is the generator of the various egg carton surface patterns mentioned above and hence we use a framework that has intrinsic diversity that matches the geometric diversity. The director is defined as a unit vector on the unit sphere $\mathbf{n} \in S^2$, where $\mathbf{n} \sim -\mathbf{n}$. Hence it is natural to express the three components in a spherical coordinate system. Without losing generality, a reference director field $\bar{\mathbf{n}}$ is defined by

$$\bar{\mathbf{n}} = \begin{bmatrix} \sin\bar{\phi}\,\cos\bar{\theta} \\ \cos\bar{\phi}\,\cos\bar{\theta} \\ \sin\bar{\theta} \end{bmatrix}. \tag{3}$$

The director field $\mathbf{n}$ is a 3D vector parametrized by $(\bar{\theta}, \bar{\phi})$. The relationship between $(\bar{\theta}, \bar{\phi})$ coordinate to a usual spherical coordinate system with polar angle θ and azimuthal angle ϕ is given by the following transformations:

$$\bar{\phi} = -\phi - \frac{\pi}{2}, \quad \bar{\theta} = \theta + \frac{\pi}{2}. \tag{4}$$

For a perfect cholesteric N* liquid crystal, we expect $\bar{\phi}$ and $\bar{\theta}$ to be linearly dependent on x and y or vice versa. To discuss all possibilities that include nematics and cholesterics, we assume without loss of generality $\bar{\phi} = ax$, $\bar{\theta} = by$ for a linear and spatially decoupled director field and apply the permutation group to obtain all possibilities. Here $aP_{0x} = bP_{0y} = 2\pi$, where P_{0x} and P_{0y} are the helix pitches along the x and y axes, respectively.

Figure 2 shows the director field tangential projections for the six possible permutations of $\mathbf{n}$ [see Eq. (3)] on a $[0, 1] \times [0, 1]$ square in the physical (x, y) space. This important projection plot reveals the spatial distribution of splay and bend deformations [see Eq. (2)] on the (x, y)-surface

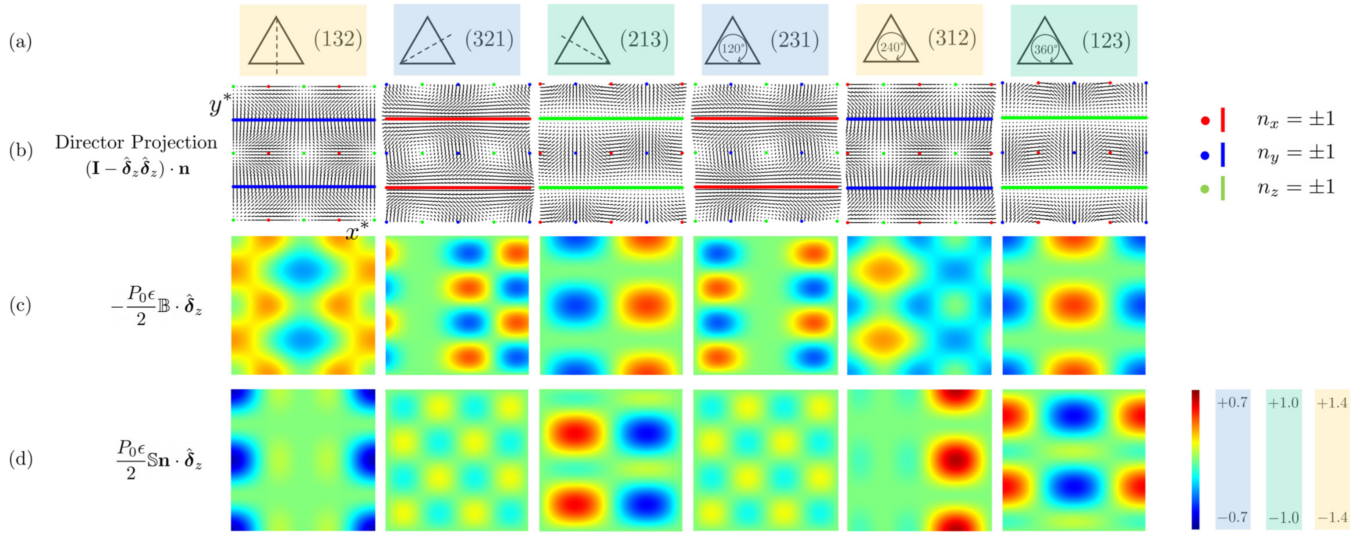

FIG. 2. Projection $(\mathbf{I} - \hat{\boldsymbol{\delta}}_z\hat{\boldsymbol{\delta}}_z) \cdot \mathbf{n}$ is a 2D vector field under which for different permutations (second row) $\mathbf{n}$ and $-\mathbf{n}$ are expected to represent the same average molecular orientation; hence no arrows are shown in the figure. Positions with green dots or lines indicate that the z component of the director is ±1 (the other two components vanish). Similarly, red color and blue color denotes the x or y component is ±1, respectively. In Eq. (14), the projections of the bending term (c) and splay term (d) under different permutations (a) demonstrate equivalence up to a translation, which leads to the same mean curvature profile (c). Each square (x^*, y^*) is $[0, 1] \times [0, 1]$ where $x^* = x/P_0$ and $y^* = y/P_0$. We use different color bar limits to preserve all details of each permutation. The color bar limits are ±0.7 (blue) for (321) and (231), ±1 (green) for (213) and (123), and ±1.4 (yellow) for (132) and (312). The anchoring coefficient is $\epsilon = -0.2$, in accordance with Fig. 7.

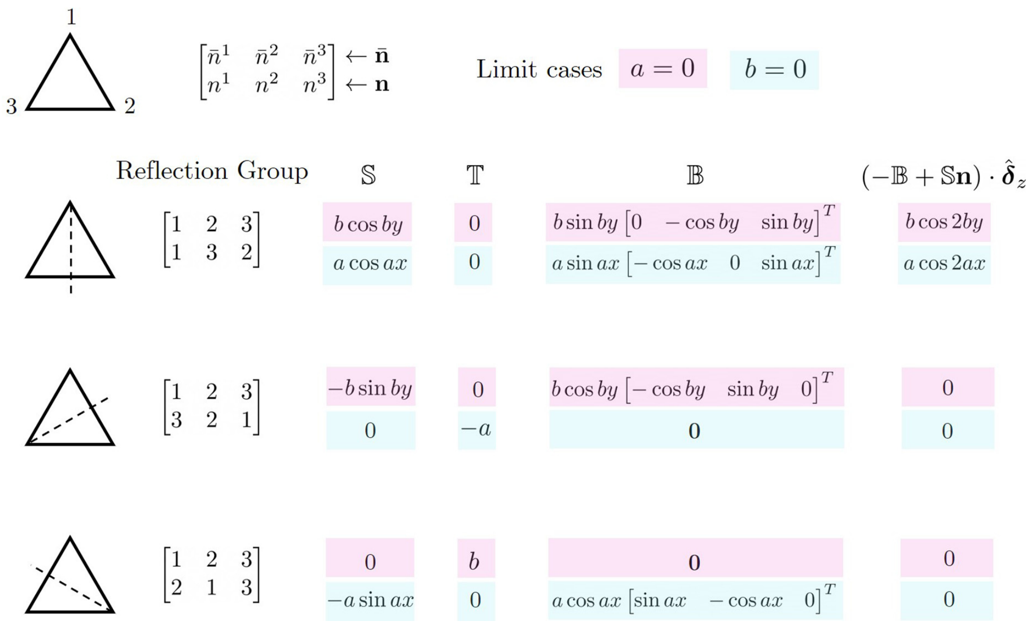

$\begin{bmatrix}\bar{n}^1 & \bar{n}^2 & \bar{n}^3\\ n^1 & n^2 & n^3\end{bmatrix}\begin{matrix}\leftarrow \bar{\mathbf{n}}\\ \leftarrow \mathbf{n}\end{matrix}$

Limit cases $a=0$ $b=0$

Reflection Group	$\mathbb{S}$	$\mathbb{T}$	$\mathbb{B}$	$(-\mathbb{B}+\mathbb{S}\mathbf{n})\cdot\hat{\boldsymbol{\delta}}_z$
$\begin{bmatrix}1&2&3\\1&3&2\end{bmatrix}$	$b\cos by$ $a\cos ax$	0 0	$b\sin by\,[0\quad -\cos by\quad \sin by]^T$ $a\sin ax\,[-\cos ax\quad 0\quad \sin ax]^T$	$b\cos 2by$ $a\cos 2ax$
$\begin{bmatrix}1&2&3\\3&2&1\end{bmatrix}$	$-b\sin by$ 0	0 $-a$	$b\cos by\,[-\cos by\quad \sin by\quad 0]^T$ 0	0 0
$\begin{bmatrix}1&2&3\\2&1&3\end{bmatrix}$	0 $-a\sin ax$	b 0	0 $a\cos ax\,[\sin ax\quad -\cos ax\quad 0]^T$	0 0

FIG. 3. Limit cases $a=0$ and $b=0$ of splay $\mathbb{S}$, twist $\mathbb{T}$, bend $\mathbb{B}$, and the splay-bend combinations [Eq. (14)] for three reflection permutations.

lattice corresponding to each of the six permutations. The color associated with each permutation defines equivalence; for example, yellow on the top row corresponds to permutations (132) and (312).

If one component of the director field is ±1, then the other two must vanish due to the constraint $\mathbf{n}^2 = 1$. Specially, if the z component of the director is ±1 [green dots and lines in Fig. 2(b)], director escape occurs, which is an important concept to study the liquid crystal nonsingular defects. The red (average orientation aligns horizontally) or blue (average orientation aligns vertically) dots or lines represent x or y component is ±1, respectively. The coordinates for the dots are $x^* = 0$, 1/4, 1/2, 3/4, and 1, while $y^* = 0$, 1/2, and 1. The lines are $y^* = 1/4$ and 3/4. The difference between (132) and (312) is that the red and blue dots switch their roles. The other equivalent permutations behave in a similar way.

In this paper the director field is nonsingular but director escape ($n_z = \pm 1$) is always present. The permutations (213) and (123) show a pattern of splay-bend walls interrupted by horizontal bandlike regions of director escape ($n_z = \pm 1$) into the third dimension (here along the surface normal). The other permutations show patterns with localized director escape and a balance of centers and saddles [(132) and (312)], or a balance of saddles and sinks or sources [(321) and (231)]. Below we show how these clearly different director deformation patterns result in a rich diversity of egg cartons, containing mixtures of uniaxial, equibiaxial, and biaxial wrinkling patterns.

Figures 2(c) and 2(d) are the projected bending term and projected splay term, respectively. Figure 2 reveals that, for a given reflection permutation, there is always a rotation permutation which generates the same results. Crucially important, we show below that those two equivalent permutations share the same z component, showing the impact of orientation along the escape direction. The translational symmetries between (132) and (312), (321) and (231), and (213) and (123) imply that they represent an equivalent molecular field due to their periodicity. Thus they should generate the same surface wrinkling profiles, which will be proven below while discussing Fig. 7. The translational invariance between a reflection permutation and a rotation permutation presented in Fig. 2 is given in Eq. (15).

By comparing (c) and (d) in Fig. 2, we observe that the maxima and minima in (321) and (231) are in phase such that higher values (red area) in (c) also correspond to higher values in (d) and the same for lower values. While in (213) and (123), (132) and (312) the phenomenon is out of phase such that higher or lower values in (c) correspond to zero (green area) in (d).

The permutations of the nonsingular director are categorized by reflection permutations (Fig. 3) and rotation permutations (Fig. 4), shown in the first and second column on both figures. The next four columns show the splay,

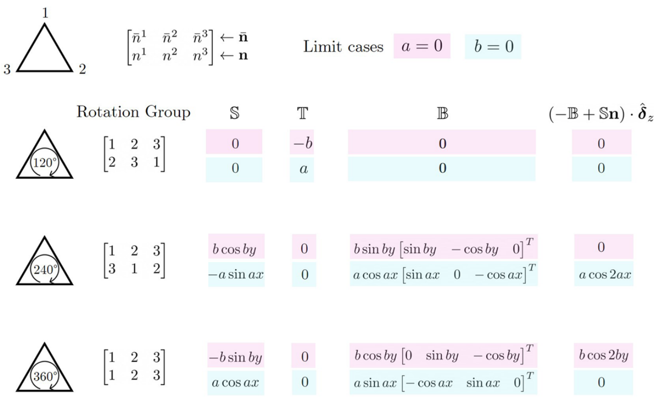

$\begin{bmatrix}\bar{n}^1 & \bar{n}^2 & \bar{n}^3\\ n^1 & n^2 & n^3\end{bmatrix}\begin{matrix}\leftarrow \bar{\mathbf{n}}\\ \leftarrow \mathbf{n}\end{matrix}$

Limit cases $a=0$ $b=0$

Rotation Group	$\mathbb{S}$	$\mathbb{T}$	$\mathbb{B}$	$(-\mathbb{B}+\mathbb{S}\mathbf{n})\cdot\hat{\boldsymbol{\delta}}_z$
$\begin{bmatrix}1&2&3\\2&3&1\end{bmatrix}$	0 0	$-b$ a	0 0	0 0
$\begin{bmatrix}1&2&3\\3&1&2\end{bmatrix}$	$b\cos by$ $-a\sin ax$	0 0	$b\sin by\,[\sin by\quad -\cos by\quad 0]^T$ $a\cos ax\,[\sin ax\quad 0\quad -\cos ax]^T$	0 $a\cos 2ax$
$\begin{bmatrix}1&2&3\\1&2&3\end{bmatrix}$	$-b\sin by$ $a\cos ax$	0 0	$b\cos by\,[0\quad \sin by\quad -\cos by]^T$ $a\sin ax\,[-\cos ax\quad \sin ax\quad 0]^T$	$b\cos 2by$ 0

FIG. 4. Limit cases $a=0$ and $b=0$ of splay $\mathbb{S}$, twist $\mathbb{T}$, bend $\mathbb{B}$, and the splay-bend combinations [Eq. (14)] for three rotation permutations.

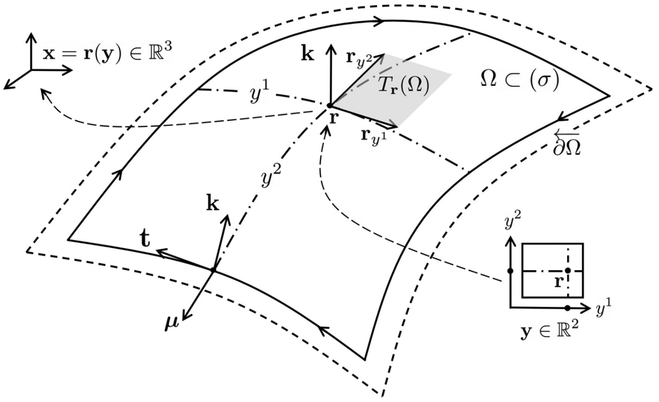

FIG. 5. Schematic of basic parameters on surface geometry. $\mathbf{r}_\alpha$ ($\alpha = y^1, y^2$) are the local tangent vectors at point $\mathbf{r} \in \mathbb{R}^3$ and $T_\mathbf{r}(\Omega)$ is the tangent surface span$\{\mathbf{r}_\alpha\}$. $\mathbf{k}$ is the surface unit normal. $\overleftarrow{\partial\Omega}$ is the oriented boundary, with unit tangent vector $\mathbf{t}$ and outward normal $\boldsymbol{\mu}$.

twist, bend, and splay-bend combination $(-\mathbb{B} + \mathbb{S}\mathbf{n}) \cdot \hat{\boldsymbol{\delta}}_z$ under wave-vector extrema: pink for $a = 0$ and blue for $b = 0$. As will be shown below in the linear regime the effective capillary pressure is $(-\mathbb{B} + \mathbb{S}\mathbf{n}) \cdot \hat{\boldsymbol{\delta}}_z$ and hence its extrema provides a reference to discuss and classify the results (see Figs. 6 and 7).

In partial summary, in this section we have introduced a generic and versatile method to describe various surface director fields with the potential to generate a range of egg carton surfaces (uniaxial, equibiaxial, and biaxial). Furthermore, symmetry relations in the material surface space were identified and will be used below.

C. Intrinsic geometric approach

An intrinsic differential geometric approach is applied to study egg carton surface wrinkling patterns. Figure 5 is an intuitive schematic showing the basic geometric parameters. The formal parameter definitions are provided in Appendix A. The adopted notations follow [53]. In Fig. 5, we define (σ) as the surface being studied and Ω as a small surface patch with oriented boundary $\overleftarrow{\partial\Omega}$. $\mathbf{k}$ is the surface unit normal on a local surface patch and $\mathbf{r}_\alpha$ are the two local tangent vectors on the curvilinear coordinate system y^α. $(\mathbf{k}, \mathbf{r}_\alpha)$ form a local coordinate system with $\mathbf{k} \perp \mathbf{r}_\alpha$.

$\nabla_{(\sigma)}$ is the surface gradient operator $\nabla_{(\sigma)} = \mathbf{r}_\alpha \mathbf{r}^\alpha \cdot \boldsymbol{\nabla}$, where $\mathbf{r}^\alpha$ is the dual vector of $\mathbf{r}_\alpha$. The curvature tensor $\mathbf{B} = -\nabla_{(\sigma)}\mathbf{k}$ has real eigenvalues κ_1 and κ_2. Mean H, Gaussian K, deviatoric D, and Casorati C curvatures, along with the dimensionless shape parameter S [54], are summarized in Table I, together with their physical significance and special cases for zero curvatures and special cases for the shape parameter S. For example, the shape parameter S is a scalar whose magnitude and sign defines the shape of the surface patch, while the Casorati curvature C is a non-negative scalar that indicates deviation from a flat surface.

$\mathbf{t}$ and $\boldsymbol{\mu}$ are the unit vectors on the boundary $\overleftarrow{\partial\Omega}$, such that both $\mathbf{t}$ and $\boldsymbol{\mu}$ are in the tangent space $T_\mathbf{r}(\Omega)$ and $(\mathbf{t}, \mathbf{k}, \boldsymbol{\mu})$ is a local orthonormal vector triad.

Finally we define the tensor index notation as $\nabla_i A_j = (\boldsymbol{\nabla} A)_{ij}$, $(A_{ij})^T = A_{ji}$, and $\mathbf{A} : \mathbf{B} = A_{ij}B_{ji}$. The Einstein notation is used throughout the research.

D. Governing shape equation

The solution to the governing equation generates different surface wrinkling patterns. In this section, two different models are proposed based on the director field $\mathbf{n}$. The full director model separates the information of geometry ($\mathbf{k}$, $\nabla_{(\sigma)}$) and material physics ($\mathbf{n}$, ϵ). The 3D Cahn-Hoffman capillary vector is defined by the spatial derivative of the product of the position and local surface tension [55,56], which can be decomposed into the surface normal direction $\mathbf{k}$ and the plane defined by the two tangent vectors $\mathbf{r}_1$ and $\mathbf{r}_2$ [Eq. (A1)]:

$$\boldsymbol{\xi} = \boldsymbol{\nabla}(|r|\gamma(\mathbf{k})) = \underbrace{\gamma\mathbf{k}}_{\boldsymbol{\xi}_\perp} + \underbrace{\mathbf{I}_{(\sigma)} \cdot \frac{\partial\gamma}{\partial\mathbf{k}}}_{\boldsymbol{\xi}_\parallel}. \tag{5}$$

The Cahn-Hoffman capillary vector considers the anisotropic effect brought by $\boldsymbol{\nabla}\gamma$, whose value vanishes for an isotropic surface ($\boldsymbol{\xi}_\parallel = \mathbf{0}$) and $\boldsymbol{\xi} = \gamma_0\mathbf{k}$. The Cahn-Hoffman vector serves as the anisotropic surface normal vector, related to weighted mean curvature p_c [57], which is also the pressure jump on the surface

$$\nabla_\sigma \cdot \boldsymbol{\xi} = p_c. \tag{6}$$

The capillary pressure p_c is balanced by the bulk stress jump $\mathrm{SJ} = \mathrm{SJ}(f_b, \mathbf{k}, \nabla_{(\sigma)}\mathbf{n}, \nabla_\perp\mathbf{n})$, which is dependent on both surface gradient $\nabla_{(\sigma)}$ and normal gradient $\nabla_\perp$. However, it has been computed that stress jump SJ contributes less than 2% to the governing equation for a biological cholesteric liquid

TABLE I. Principal curvatures contain various information to characterize the surface geometry.

Curvature	Notation	Significance	Expression[a]	Special case (= 0)
Mean	H	Average value	$\frac{\kappa_1+\kappa_2}{2}$	Saddle
Gaussian	K	Intrinsic	$\kappa_1\kappa_2$	Cylinder
Deviatoric	D	Sphericity	$\frac{\kappa_1-\kappa_2}{2} > 0$	Sphere
Casorati	C	Magnitude	$\sqrt{\frac{\kappa_1^2+\kappa_2^2}{2}} > 0$	Flat
Shape parameter	S	Shape	$\frac{2}{\pi}\arctan\left(\frac{\kappa_1+\kappa_2}{\kappa_1-\kappa_2}\right)$	$\begin{cases} = 0, \text{ saddle} \\ = \pm 0.5, \text{ cylinder} \\ = \pm 1, \text{ sphere} \end{cases}$

[a] Assume $\kappa_1 > \kappa_2$.

crystal system with typical pitch $P_0 > 1$ µm [58]. In this research, we study the periodic solution to the easy shape such that $p_c = 0$. Equation (6) also minimizes the surface free energy with detailed derivations given in [59,60].

The expansion to Eq. (6) results in

$$-p_c = -\nabla_{(\sigma)}\cdot\boldsymbol{\xi} = \underbrace{-\frac{\partial\boldsymbol{\xi}_\perp}{\partial\mathbf{k}}:(\nabla_{(\sigma)}\mathbf{k})^T}_{\text{dilation pressure}} \underbrace{-\frac{\partial\boldsymbol{\xi}_\parallel}{\partial\mathbf{n}}:(\nabla_{(\sigma)}\mathbf{n})^T}_{\text{director pressure}} \underbrace{-\frac{\partial\boldsymbol{\xi}_\parallel}{\partial\mathbf{k}}:(\nabla_{(\sigma)}\mathbf{k})^T}_{\text{rotation pressure}}. \tag{7}$$

The molecular orientation of liquid crystal does not have a preference on $\mathbf{n}$ or $-\mathbf{n}$, i.e., $\mathbf{n}$ and $-\mathbf{n}$ should generate the same result. This can be verified by performing a reflection in Eqs. (1), (2), (5), (6), and (7).

1. *Full director model (global)*

Replacing $\boldsymbol{\xi}_\parallel$ and $\boldsymbol{\xi}_\perp$ [from Eq. (5) to Eq. (7)], we obtain the full director model (full derivation in Appendix B)

$$\frac{p_c}{\gamma_0} = [\epsilon(\mathbf{n}\cdot\mathbf{k})^2 - 2]H + \epsilon[\mathbf{kn}:\nabla_{(\sigma)}\mathbf{n} + (\mathbf{n}\cdot\mathbf{k})\,\mathrm{tr}(\nabla_{(\sigma)}\mathbf{n}) - \mathbf{nn}:\mathbf{B}]. \tag{8}$$

If we apply the Monge parametrization [19] in Eq. (8) such that the surface relief is $h = h(x, y)$, where (x, y, z) is the common fixed laboratory coordinate system and h is along the z axis, the complete governing equation (8) takes the form of Eq. (B13), given in Appendix B. In this paper we study only the case of $p_c = 0$. Taking into account hydrodynamic mode, elastic Frank elasticity corrections, Marangoni flows, and active stresses may yield higher complexity, but these effects are beyond the scope of this work.

2. *Local director field decomposition*

In Sec. II D 1, the components n^i of the director field $\mathbf{n}$ is described in a global orthonormal coordinate system $\{\mathbf{e}_i\}$. There also exists a moving coordinate system $\{\mathbf{r}_\alpha, \mathbf{k}\}$ on the wrinkled surface, which induces a decomposition along the tangent plane and the surface normal direction:

$$\mathbf{n} = \mathbf{I}\cdot\mathbf{n} = \mathbf{I}_{(\sigma)}\cdot\mathbf{n} + \mathbf{kk}\cdot\mathbf{n} = n_\parallel^\alpha\mathbf{r}_\alpha + n_\perp\mathbf{k} \tag{9}$$

and generates a special term in director pressure that precisely cancels the rotation pressure such that the governing shape equation reduces to (derivation in Appendix C)

$$-p_c = 2H\gamma - \epsilon\gamma_0\nabla_{(\sigma)}\cdot\mathcal{N}, \tag{10}$$

where $\mathcal{N} = n_\perp\mathbf{n}_\parallel$ is a tangential vector field on the surface. Applying $2H = -\nabla_{(\sigma)}\cdot\mathbf{k}$ to Eq. (10) gives

$$p_c = \gamma\nabla_{(\sigma)}\cdot\mathbf{k} + \epsilon\gamma_0\nabla_{(\sigma)}\cdot\mathcal{N} \tag{11}$$

$$= \nabla_{(\sigma)}\cdot(\gamma\mathbf{k} + \epsilon\gamma_0\mathcal{N}) - \underbrace{\mathbf{k}\cdot\nabla_{(\sigma)}\gamma}_{0}, \tag{12}$$

which is equivalent to $p_c = \nabla_{(\sigma)}\cdot\boldsymbol{\xi}$ by replacing $\boldsymbol{\xi}_\perp = \gamma\mathbf{k}$ and $\boldsymbol{\xi}_\parallel = \epsilon\gamma_0\mathcal{N}$. Equation (10) has a simpler form than Eq. (8), since the geometry-physics information are entangled in the $\mathcal{N}$ vector. In a moving coordinate system $\{\mathbf{r}_\alpha, \mathbf{k}\}$, the rotation information ($\partial_\mathbf{k}$) naturally disappears. The anisotropic effect is absorbed in the director term (dependent on $\nabla_{(\sigma)}\mathbf{n}$ only) and becomes an effective director pressure (dependent on both $\nabla_{(\sigma)}\mathbf{n}$ and $\nabla_{(\sigma)}\mathbf{k}$).

In partial summary, our goal is to find the relationship between the geometry ($\mathbf{k}$) and the director field ($\mathbf{n}$). We solve Eq. (8) in a forward problem ($\mathbf{n} \to \mathbf{k}$). We note that Eq. (10) is an inverse problem to find director orientation given the geometry ($\mathbf{k} \to \mathbf{n}$).

3. *Linear shape equation model*

Weak anchoring ($\epsilon \to 0$) results in small wrinkling ($\boldsymbol{\nabla}h \approx \mathbf{0}$). We keep the curvature information ($\boldsymbol{\nabla\nabla}h$) and neglect the surface gradient term ($\boldsymbol{\nabla}h = \mathbf{0}$) to obtain a linearized model. In Monge parametrization $h(x, y)$ the linearized governing equation takes the form ($p_c = 0$)

$$h_{xx} + h_{yy} = \epsilon\big[n^1n_x^3 + n^2n_y^3 + n^3(n_x^1 + n_y^2)\big], \tag{13}$$

which is a Poisson equation. In this work we seek periodic solutions (that can be analytically solved by Fourier transform) to Eq. (13). We recall that Eq. (13) is the linearized version of the easy shape equation, and demonstrates that nontrivial shapes in N/N* interfaces arise whenever $\epsilon[n^1n_x^3 + n^2n_y^3 + n^3(n_x^1 + n_y^2)]$ is not zero.

Notably, Eq. (13) can also be written in terms of the splay and bend contributions appearing in Eq. (2):

$$2H = \epsilon(-\mathbb{B} + \mathbb{S}\mathbf{n})\cdot\hat{\boldsymbol{\delta}}_z. \tag{14}$$

Equation (14) shows that the mean curvature H is independent of the twist deformation and is linear in $(-\mathbb{B} + \mathbb{S}\mathbf{n})\cdot\hat{\boldsymbol{\delta}}_z$. A minimal surface will be generated if the vector $-\mathbb{B} + \mathbb{S}\mathbf{n}$ is completely on the (x, y) plane.

Equation (13) demonstrates the unique role the n^3 component plays in wrinkling phenomenon. Permutations sharing the same n^3 component generate the same result due to the fact that other terms in Eq. (13) are also the same up to a trivial translation, which was previously confirmed by Fig. 2.

E. Numerical methods

We formulate and implement a numerical solution to Eq. (8) [see Eq. (B13) in the Monge parametrization]. The input variables are the director field [Eq. (3)] and the anchoring coefficient ϵ. We use a pseudotransient method [61–63] to compute the steady state solution and the EPS approach [61] to treat the implicit Euler step. The advantage of using a pseudotransient method is that it avoids evaluating a singular Jacobian ($\det\mathbf{J} = 0$) when $h = 0$ is a trivial solution [or $(-\mathbb{B} + \mathbb{S}\mathbf{n})\cdot\hat{\boldsymbol{\delta}}_z$ vanishes].

We use the periodic boundary condition to compute the first and second spatial derivatives for each time step. The helix pitch $P_0 = 1$ (units: length) and $a = b = 2\pi$ (units: 1/length) for N* or lattice size for N. A 500×500 evenly distributed mesh and time step $dt = 10^{-8} \ll dx = dy \approx 2 \times 10^{-3}$ are applied to fulfill the standard von Neumann stability. The initial condition for the governing nonlinear shape PDE is assumed to be $10^{-3}\,\mathrm{rand}(0, 1)$. The EPS parameter [61] is $\epsilon_0 = 10^{-5}$, with tolerance $\tau \sim 10^{-6}$ and the time parameter $\omega = dt/(dt + \epsilon_0)$. Quantitative validation at the steady state of the numerical solution are established by systematic

TABLE II. Splay-bend combination of each permutation.

Permutation	$(-\mathbb{B}+\mathbb{S}\mathbf{n})\cdot\hat{\boldsymbol{\delta}}_z/\pi$
Reflection (132)	$2\,\cos 4\pi x^*\cos^2 2\pi y^* + 2\,\cos 2\pi x^*\cos 4\pi y^*$[a]
Reflection (321)	$\cos 2\pi x^*\sin 4\pi y^* - \sin 4\pi x^*\sin 4\pi y^*$
Reflection (213)	$2\,\sin 2\pi x^*\cos 4\pi y^* + \sin 2\pi x^*\sin 4\pi y^*$
Rotation (231)	$-\sin 2\pi x^*\sin 4\pi y^* - \sin 4\pi x^*\sin 4\pi y^*$
Rotation (312)	$2\,\sin 2\pi x^*\cos 4\pi y^* + 2\,\cos 4\pi x^*\cos^2 2\pi y^*$
Rotation (123)	$\cos 2\pi x^*\sin 4\pi y^* + 2\,\cos 2\pi x^*\cos 4\pi y^*$

[a] Dimensionless spatial variables $x^* = x/P_0$ and $y^* = y/P_0$.

agreements with available solutions to the linearized model (Table III).

III. RESULTS AND DISCUSSION

In this section, we present, characterize, and analyze the numerical solutions to the governing equation [Eq. (B13)] in Sec. III A and the curvature profiles in Sec. III B.

A. Surface relief

We summarize the values for all six director permutations into Table II and Fig. 6. We use an ordered pair (ω_x, ω_y) to represent the frequency along the x and y axes, respectively, and it corresponds to a sinusoidal wave patch $\sim e^{2\pi i(\omega_x x+\omega_y y)}$. We note that $\omega_x = 0$, $\omega_y = 0$ implies a translation $h = h +$ const [a symmetry that arises from Eq. (8)] and it does not affect the pattern and is not considered further.

Table II and Fig. 6 reveal frequency-related features of all possible surface relief profiles. The polar angle θ and azimuthal angle ϕ from Eq. (3) are taken in different ranges in the spherical coordinate system with translated dimensionless surface coordinates $ax = \bar{\theta} \in [0, \pi]$ and $by = \bar{\phi} \in [0, 2\pi]$. An asymmetric wave patch $\omega_y = 2\omega_x$ naturally arises by equating $a = b = 2\pi$. In Table II, the asymmetry exists for all permutations and contributes the most for all permutations.

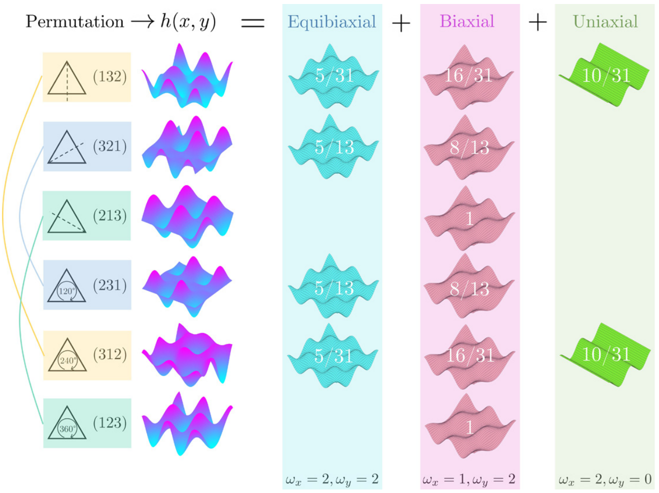

FIG. 6. Summary of surface patterns for the six director permutations and their mode decomposition. The value demonstrates the contribution of each mode based on Table III. Permutations (left column) with the same color are equivalent.

If $a \neq b$, then we do not expect to observe any ideal egg carton surface. Hence, throughout this research, $a = b$ is desired for revealing the contribution of an ideal egg carton mode to the surface wrinkling profile.

Figure 6 is the decomposition figure for all director permutations. The surface profile for each permutation group is shown in the $h(x, y)$ column. Each surface profile can be decomposed into three fundamental modes: equibiaxial, biaxial, and uniaxial egg carton patterns. Permutations connected by the same color demonstrate that they are equivalent up to a trivial translation. The numerical values on each mode present the contribution of each fundamental mode (Table III). Notably, Fig. 6 shows that permutations (123) and (213) yield a purely biaxial egg carton, while permutations (132) and (312) yield a ternary mixture of egg cartons, differences caused by the spatial distribution of splay and bend deformations. Table II and Eq. (14) provide a tool to solve the linearized analytical solution [accuracy $h_{\text{exact}} = h_{\text{linear}} + O(|\nabla h|)$]. The solutions are summarized in Table III.

There are three frequencies observed in Table II, Table III, and Fig. 6, related to particular egg cartons, as follows.

(i) $(\omega_x = 2, \omega_y = 2)$: equibiaxial egg carton pattern, which cannot be seen from reflection (213) and rotation (123).

(ii) $(\omega_x = 1, \omega_y = 2)$: biaxial egg carton pattern, which originates from the asymmetric roles played by the azimuthal angle and polar angle in the spherical coordinate system. $(\omega_x = 1, \omega_y = 2)$ can be observed in all six permutations and is a universal wave pattern under the condition of $a = b$.

(iii) $(\omega_x = 2, \omega_y = 0)$: uniaxial (ideal) egg carton pattern with vanishing Gaussian curvature. This type of 1D wrinkling comes from the fact that a sine or cosine wave multiplied by itself (without phase shift), whose net effect is equivalent to a constant plus a sinuous wave with doubled frequency due to $\cos^2\theta = (\cos 2\theta + 1)/2$.

Table II and Eq. (14) also show that, as long as $(-\mathbb{B} + \mathbb{S}\mathbf{n})\cdot\hat{\boldsymbol{\delta}}_z$ is invariant under translation $x \rightarrow x + c$ and $y \rightarrow y + c$, the surface patterns are equivalent within the linear region. We can observe that, by performing the following translation, every reflection group has a corresponding rotation group that generates a similar pattern,

$$\begin{aligned}
\text{Ref (132)} \rightarrow \text{Rot (312)} &: (x^*, y^*) \rightarrow (x^* + 1/4, y^*),\\
&\quad h^* \rightarrow -h^*,\\
\text{Ref (321)} \rightarrow \text{Rot (231)} &: (x^*, y^*) \rightarrow (x^* - 1/4, y^*),\\
&\quad h^* \rightarrow -h^*,
\end{aligned}$$

TABLE III. Analytic solution of $h = h_{\text{linear}} + O(|\nabla h|)$ [computed from Eq. (14)].

Permutation	$-\pi h^*_{\text{linear}}/\epsilon$
Reflection (132)	$\frac{1}{32}\cos 4\pi x^* \cos 4\pi y^* + \frac{1}{16}\cos 4\pi x^* + \frac{1}{10}\cos 2\pi x^* \cos 4\pi y^*$[a]
Reflection (321)	$\frac{1}{20}\cos 2\pi x^* \sin 4\pi y^* - \frac{1}{32}\sin 4\pi x^* \sin 4\pi y^*$
Reflection (213)	$\frac{1}{10}\sin 2\pi x^* \cos 4\pi y^* + \frac{1}{20}\sin 2\pi x^* \sin 4\pi y^*$
Rotation (231)	$-\frac{1}{20}\sin 2\pi x^* \sin 4\pi y^* - \frac{1}{32}\sin 4\pi x^* \sin 4\pi y^*$
Rotation (312)	$\frac{1}{10}\sin 2\pi x^* \cos 4\pi y^* + \frac{1}{16}\cos 4\pi x^* + \frac{1}{32}\cos 4\pi x^* \cos 4\pi y^*$
Rotation (123)	$\frac{1}{20}\cos 2\pi x^* \sin 4\pi y^* + \frac{1}{10}\cos 2\pi x^* \cos 4\pi y^*$

[a] Dimensionless spatial variables $x^* = x/P_0$, $y^* = y/P_0$, and $h^* = h/P_0$.

$$\text{Ref (213)} \rightarrow \text{Rot (123)} : (x^*, y^*) \rightarrow (x^* + 1/4, y^*),\quad h^* \rightarrow +h^*, \tag{15}$$

from which we verify again that x and y do not play a symmetric role.

In partial summary, numerical solutions validated with the linear solutions shows that the director field **n** in Eq. (3) generates all possible egg cartons: uniaxial, biaxial, and equibiaxial that superpose according to the symmetry of the director field. The single mode biaxial egg carton pattern arises when n^3 is only periodic in y; otherwise the shape is a superposition of the three primitive egg cartons (uniaxial, biaxial, and equibiaxial). The Fourier method was instrumental in mode decoupling. The linear model (Table III) sheds light on the origin of these modes. Finally, Eq. (15) reveals the equivalence of rotation or translation dual modes.

B. Curvature distribution

As noted above the surface curvature tensor is a symmetric second order tensor $\mathbf{B} = -\nabla_{(\sigma)}\mathbf{k}$, with real eigenvalues κ_1 and κ_2 as the two principal curvatures. The **B** tensor contains the second derivative information on the space. The tensor invariants $\operatorname{tr}\mathbf{B}$ and $\det\mathbf{B}$ determine two independent curvatures—the mean curvature H and Gaussian curvature K. Table I summarizes several curvatures and we only need H and G to determine the rest with $D = \sqrt{H^2 - K}$, $C = \sqrt{H^2 + D^2}$, and $S\pi = 2\arctan(H/D)$.

The dimensionless curvature P_0H, Gaussian curvature P_0^2K, Casorati curvature P_0C, and the dimensionless shape parameter S for reflection groups are summarized in Fig. 7. From Eq. (14) and Table II, we can analytically solve the curve L_H along which mean curvature P_0H vanishes. $P_0H = 0$ corresponds to a local minimal surface as per calculus of variation, depicted as white curves in the third column of Fig. 7. For the (132) permutation, L_H are white curves are defined by

$$L_H^{(132)}: \quad 2\pi y^* = \arccos\left(\sqrt{\frac{\cos 2\pi x^*}{2\cos^2 2\pi x^* + 2\cos 2\pi x^* - 1}}\right).$$

For (321) and (213) permutation, L_H are straight lines and they are superposed on Fig. 7 as white rectangles. The green color for (213) permutation does not overlap with the white rectangles $L^{(213)}$. This result demonstrates that h and its first derivative ∇h can be linearly approximated; nevertheless, the second derivative $\nabla\nabla h$ shows a significant nonlinearity.

Mean curvature $H = \nabla^2 h + O(|\nabla h|^2)$ admits additivity such that $H = \sum_i a_i H_i$ if h can be decomposed according to different modes $h = \sum_i a_i h_i$. The mean curvature plots in Fig. 7 are also the consequence by superposing the mean curvature plots of its corresponding modes from Fig. 6.

The Gaussian curvature is an intrinsic curvature. $P_0^2K = 0$ denotes a local developable surface (uniaxial). (321) surface does not have contributions from a uniaxial patch from Fig. 6; however, most of the surfaces are developable by comparing the green area. Gaussian curvature is given by $K = \det(\nabla\nabla h) + O(|\nabla h|^2)$ and hence it does not admit additivity. (213) is the Gaussian curvature map of a pure biaxial egg carton surface from Fig. 6.

The Casorati curvature measures the absolute magnitude of two principal curvatures. The deep blue color represents the flat surface region and the deep red color represents the surface with more bending. The extensive developable region in (321) surface demonstrates $P_0C = 0$; hence they are also flat, due to the cancellation of equibiaxial egg carton mode and biaxial egg carton mode from Fig. 6. In general, (132) is the most curved and (321) is the flattest among the three reflection groups.

The shape parameter S is by definition dimensionless. Both deep blue and deep red indicate a spherical patch with the opposite direction, and they contact with each other in Fig. 7. The contacting points are locations where principal curvatures start to change sign, i.e., a local cylindrical patch, and that is the reason that yellow (cyan) curves ($S = \pm 0.5$) exactly follow the same cyan curve shown in the Gaussian map. The value of $S = 0$ indicates a saddle patch. The S results follow the shape transition rules that when moving from a spherical cup to a spherical dome we must encounter cylindrical cups, saddles, and cylindrical domes.

By comparing Fig. 7 and Table III, the following symmetries are observed:

$$\begin{aligned}
\text{Ref (132)}:\quad & \frac{1}{2} - x^* \sim \frac{1}{2} + x^* \text{ (reflection symmetry)}\\
& \frac{1}{2} - y^* \sim \frac{1}{2} + y^* \text{ (reflection symmetry)},\\
\text{Ref (321)}:\quad & \frac{1}{2} - y^* \sim -\left(\frac{1}{2} + y^*\right) \text{ (centrosymmetry)},\\
\text{Ref (213)}:\quad & \frac{1}{2} - x^* \sim \left(\frac{1}{2} + x^*\right) \text{ (centrosymmetry)}.
\end{aligned} \tag{16}$$

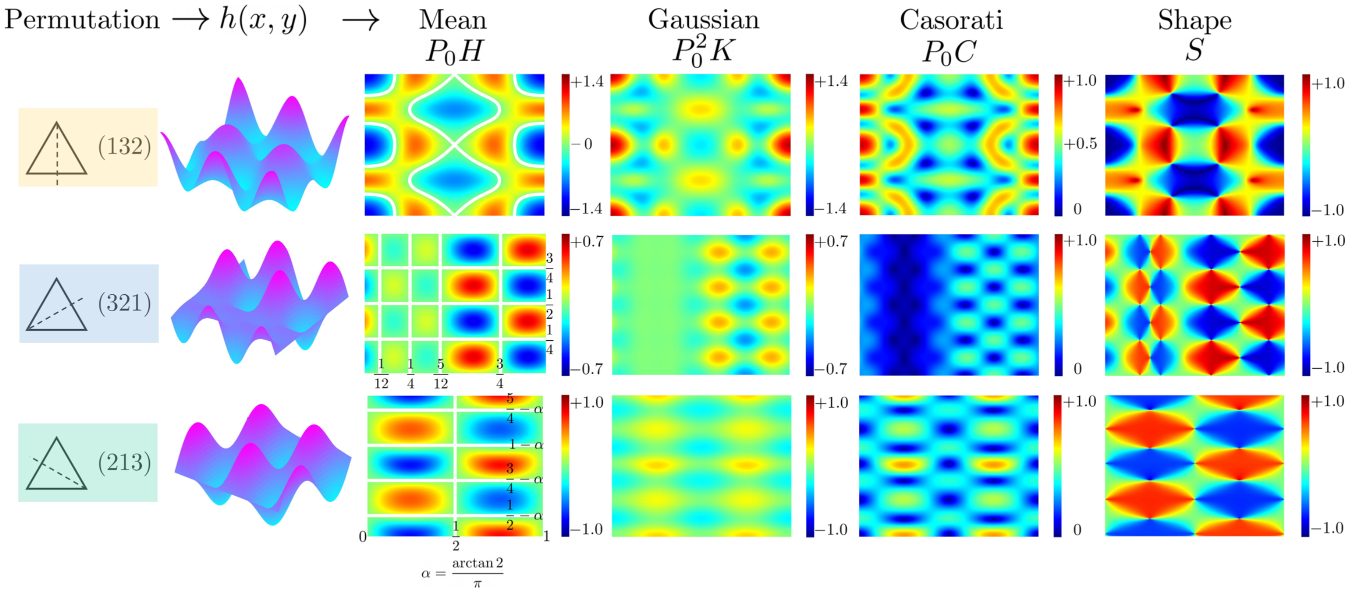

FIG. 7. Dimensionless curvature profile of three reflection groups on the (x^*, y^*) plane. Regions with vanishing curvature are demonstrated by green color. The analytic results are shown as white curves on the third column.

In partial summary, under the same anchoring conditions, the curvedness C is maximized for the three-mode surface [permutation (132)] and the largest spherical (up and down) patches are found in (213) where the n^3 has only y periodicity. On the other hand, segregated (left and right, right column middle row) large and small spherical patches are found in (321) yielding the following relative averaged features: (132): maximal curvedness, intermediate shape variability; (321): minimal curvedness, maximal shape variability; (213): intermediate curvedness, minimal shape variability.

Thus control of the director yields targeted patterns with more or less curvedness and more or less spherical or cylindrical or saddle patch transitions.

IV. SUMMARY

In this paper we formulate, solve, and characterize egg-carton-like solutions to the liquid crystal shape equation, applicable to nematic N and cholesteric N* interfaces under the absence of bulk stress jumps, a condition known as the easy shape that arises when the total capillary pressure vanishes. Complex surface shapes under zero capillary pressure, as opposed to flat or minimal surfaces, are a feature of anisotropic soft matter. The model is based on the quadratic anisotropic anchoring energy and the input is a known generic double-periodic (in x and y coordinates) director field. All symmetries and permutations of this director field are used to classify them according to effective splay-bend contributions and spatial director escape spatial organization. It is found that director escape with linear spatial organization gives rise to purely biaxial egg cartons, while latticelike source or sink orientation fields give rise to various mixtures of uniaxial, equibiaxial, and biaxial. A thorough curvature characterization identifies which director fields generate large curvedness (higher curvature amplitudes) and which generate more diverse shape gradients in terms of the spatial organization of spherical, cylindrical, and saddle patches. It is found that maximal curvedness and maximal shape diversity is found in director fields with latticelike sources and sinks. On the other hand, director fields with spatial linelike organization tend to generate lower curvedness and few and larger spherical patches. These findings contribute to additional pathways to generate potentially high functionality surfaces using intrinsic soft matter properties.

ACKNOWLEDGMENTS

This work is supported by the Natural Science and Engineering Research Council of Canada (NSERC Grant No. 223086). A.D.R. is grateful for financial support through the James McGill Professorship program at McGill University. We acknowledge Compute Canada and Calcul Québec for computational resources and technical support. Z.W. is grateful to the Faculty of Engineering of McGill University for financial support through the MEDA scholarship.

APPENDIX A: INTRINSIC DIFFERENTIAL GEOMETRY APPROACH

In this Appendix, we use an intrinsic geometric approach to describe the surface. We follow the nomenclature and approach from [53]. A point $\mathbf{r}$ on the physical surface (parametrized by two parameters $\mathbf{y} = [y^1 \quad y^2]^T$) has three spatial components: $\mathbf{r} = [x^1 \quad x^2 \quad x^3]^T$. $\mathbf{r}$ is a position map: $\mathbf{y} \mapsto \mathbf{x}$. To simplify our discussion, we require a Euclidean space $\mathbf{x} \in \mathbb{R}^3$ (with orthonormal basis $\{\hat{\boldsymbol{\delta}}_i\}$) and $\mathbf{y}$ remains in a curvilinear coordinate system (with basis $\{\mathbf{r}_\alpha\}$). In the following content, we assume Einstein summation and use Latin letters for physical coordinates ($i = 1, 2, 3$) and Greek letters for surface coordinates ($\alpha = 1, 2$).

The local tangential vectors are

$$\mathbf{r}_\alpha = \frac{\partial x^i}{\partial y^\alpha}\hat{\boldsymbol{\delta}}_i. \tag{A1}$$

The first fundamental form $\mathbf{g}$ of the surface and the metric g are defined by

$$g_{\alpha\beta} = \mathbf{r}_\alpha \cdot \mathbf{r}_\beta, \quad g = \det(\mathbf{g}), \tag{A2}$$

with the inverse and dual vectors

$$g^{\alpha\beta} = g^{-1}_{\alpha\beta}, \quad \mathbf{r}^\alpha = g^{\alpha\beta}\mathbf{r}_\beta. \tag{A3}$$

The unit normal vector $\mathbf{k}$

$$\mathbf{k} = \frac{\mathbf{r}_{y^1} \times \mathbf{r}_{y^2}}{\|\mathbf{r}_{y^1} \times \mathbf{r}_{y^2}\|}. \tag{A4}$$

Denote T^n the nth order tensor product space. The surface gradient operator $\nabla_{(\sigma)} : T^n \mapsto T^{n+1}$ is defined by

$$\nabla_{(\sigma)} = \mathbf{r}^\beta \nabla_{(\sigma)\beta} = \mathbf{r}_\alpha g^{\alpha\beta}\nabla_{(\sigma)\beta} = \mathbf{r}_\alpha \nabla^\alpha_{(\sigma)} = \mathbf{r}_\alpha \mathbf{r}^\alpha \cdot \boldsymbol{\nabla}, \tag{A5}$$

where $\nabla^\alpha_{(\sigma)}$ is dual to $\nabla_{(\sigma)\alpha}$.

Therefore, given that $\mathbf{n} = n^i \mathbf{e}_i$, the surface gradient of the director yields a 2×3 matrix

$$\nabla_{(\sigma)}\mathbf{n} = \nabla^\alpha_{(\sigma)} n^i \mathbf{r}_\alpha \hat{\boldsymbol{\delta}}_i = \nabla_{(\sigma)\beta} n^j \mathbf{r}^\beta \hat{\boldsymbol{\delta}}_j. \tag{A6}$$

Therefore, the trace of a second order tensor $\mathrm{tr} : T^2 \mapsto \mathbb{R}$ is equivalent to the surface divergence $\nabla_{(\sigma)} \cdot : T^n \mapsto T^{n-1}$ when $n = 1$:

$$\mathrm{tr}(\nabla_{(\sigma)}\mathbf{n}) = \nabla_{(\sigma)} \cdot \mathbf{n} = \nabla^\alpha_{(\sigma)} n^i (\mathbf{r}_\alpha \cdot \hat{\boldsymbol{\delta}}_i) = \nabla_{(\sigma)\beta} n^j (\mathbf{r}^\beta \cdot \hat{\boldsymbol{\delta}}_j). \tag{A7}$$

The surface curvature tensor $\mathbf{B}$ is defined as

$$\mathbf{B} = -\nabla_{(\sigma)}\mathbf{k}, \quad H = \frac{1}{2}\,\mathrm{tr}\,\mathbf{B}, \quad K = \det \mathbf{B}. \tag{A8}$$

The normal curvature $\kappa_{\boldsymbol{\lambda}}$ along the unit tangent $\boldsymbol{\lambda} \in T_pM$ is given by

$$\kappa_{\boldsymbol{\lambda}} = \boldsymbol{\lambda}\boldsymbol{\lambda} : \mathbf{B}. \tag{A9}$$

APPENDIX B: CAHN-HOFFMAN CAPILLARY VECTOR

In this Appendix, we derive the Cahn-Hoffman capillary vector subject to the Rapini-Papoular surface energy equation [50,51].

The Cahn-Hoffman capillary vector is a map $S^2 \times S^2 \mapsto T^1$

$$\boldsymbol{\xi}(\mathbf{n}, \mathbf{k}) = \boldsymbol{\xi}_\perp + \boldsymbol{\xi}_\parallel = \gamma\mathbf{k} + \mathbf{I}_{(\sigma)} \cdot \frac{\partial \gamma}{\partial \mathbf{k}}. \tag{B1}$$

The surface divergence of $\boldsymbol{\xi}$

$$-\nabla_{(\sigma)} \cdot \boldsymbol{\xi} = -\,\mathrm{tr}\left[\mathbf{r}_\alpha g^{\alpha\beta}\nabla_{(\sigma)\beta}\boldsymbol{\xi}(\mathbf{n}, \mathbf{k})\right] \tag{B2}$$

$$= -\,\mathrm{tr}\left(\mathbf{r}_\alpha g^{\alpha\beta}\frac{\partial \boldsymbol{\xi}}{\partial n^i}\nabla_{(\sigma)\beta} n^i + \mathbf{r}_\alpha g^{\alpha\beta}\frac{\partial \boldsymbol{\xi}}{\partial k^j}\nabla_{(\sigma)\beta} k^j\right) \tag{B3}$$

$$\begin{aligned} &= \underbrace{-\frac{\partial \boldsymbol{\xi}_\perp}{\partial \mathbf{n}} : (\nabla_{(\sigma)}\mathbf{n})^T}_{0} \underbrace{-\frac{\partial \boldsymbol{\xi}_\perp}{\partial \mathbf{k}} : (\nabla_{(\sigma)}\mathbf{k})^T}_{\text{dilation pressure}} \\ &\quad \underbrace{-\frac{\partial \boldsymbol{\xi}_\parallel}{\partial \mathbf{n}} : (\nabla_{(\sigma)}\mathbf{n})^T}_{\text{director pressure}} \underbrace{-\frac{\partial \boldsymbol{\xi}_\parallel}{\partial \mathbf{k}} : (\nabla_{(\sigma)}\mathbf{k})^T}_{\text{rotation pressure}}, \end{aligned} \tag{B4}$$

where we use the tensor contraction nomenclature $\mathbf{A} : \mathbf{B} = A_{ij}B_{ji}$. $\forall(\mathbf{a}, \mathbf{b}) \in (T^1 \times T^1)$, and $\forall(\mathbf{c}, \mathbf{d}) \in (T^1 \times S^2)$; the following identities are true:

$$\mathbf{k}\mathbf{a} : (\nabla_{(\sigma)}\mathbf{b})^T = (\mathbf{k} \cdot \mathbf{r}_\alpha) g^{\alpha\beta}(\mathbf{a} \cdot \nabla_{(\sigma)\beta}\mathbf{b}) = 0, \tag{B5}$$

$$\mathbf{c}\mathbf{d} : (\nabla_{(\sigma)}\mathbf{d})^T = (\mathbf{c} \cdot \mathbf{r}_\alpha) g^{\alpha\beta}(\mathbf{d} \cdot \nabla_{(\sigma)\beta}\mathbf{d}) = 0. \tag{B6}$$

We compute the derivatives separately:

$$\frac{\partial \boldsymbol{\xi}_\perp}{\partial \mathbf{n}} : (\nabla_{(\sigma)}\mathbf{n})^T = \frac{\partial \gamma}{\partial \mathbf{n}}\mathbf{k} : (\nabla_{(\sigma)}\mathbf{n})\mathbf{r}_\alpha g^{\alpha\beta} = 0 \tag{B7}$$

and

$$\begin{aligned} \frac{\partial \boldsymbol{\xi}_\perp}{\partial \mathbf{k}} : (\nabla_{(\sigma)}\mathbf{k})^T &= \left(\frac{\partial \gamma}{\partial \mathbf{k}}\mathbf{k} + \gamma\mathbf{I}\right) : (\nabla_{(\sigma)}\mathbf{k})^T \\ &= \gamma\ \mathrm{tr}(\nabla_{(\sigma)}\mathbf{k}) = -2H\gamma. \end{aligned} \tag{B8}$$

The tangential component of the Cahn-Hoffman capillary vector is by definition

$$\boldsymbol{\xi}_\parallel = \mathbf{I}_{(\sigma)} \cdot \frac{\partial \gamma}{\partial \mathbf{k}} = W(\mathbf{n} \cdot \mathbf{k})\mathbf{I}_{(\sigma)} \cdot \mathbf{n}. \tag{B9}$$

The tensor contractions in Eq. (B4) are

$$\frac{\partial \boldsymbol{\xi}_\parallel}{\partial \mathbf{n}} : (\nabla_{(\sigma)}\mathbf{n})^T = W[\mathbf{k}\mathbf{n} : \nabla_{(\sigma)}\mathbf{n} + (\mathbf{n} \cdot \mathbf{k})\,\mathrm{tr}(\nabla_{(\sigma)}\mathbf{n})], \tag{B10}$$

$$\frac{\partial \boldsymbol{\xi}_\parallel}{\partial \mathbf{k}} : (\nabla_{(\sigma)}\mathbf{k})^T = W[\mathbf{n}\mathbf{n} : \nabla_{(\sigma)}\mathbf{k} + 2(\mathbf{n} \cdot \mathbf{k})^2 H]. \tag{B11}$$

The governing shape equation ($\epsilon = W/\gamma_0$) is

$$\begin{aligned} 0 = &\left((\mathbf{n} \cdot \mathbf{k})^2 - \frac{2}{\epsilon}\right)H + \mathbf{k}\mathbf{n} : \nabla_{(\sigma)}\mathbf{n} \\ &+ (\mathbf{n} \cdot \mathbf{k})\,\mathrm{tr}(\nabla_{(\sigma)}\mathbf{n}) - \mathbf{n}\mathbf{n} : \mathbf{B}. \end{aligned} \tag{B12}$$

To solve this equation numerically, we adopt the Monge parametrization such that $\mathbf{y} = [x \quad y]^T$ and $z = h$. If the component of the director field under orthonormal basis is n^i such that $\mathbf{n} = n^i \hat{\delta}_i$, the complete expansion of Eq. (B12) is given by Eq. (B13):

$$\begin{aligned} 0 = &\left(\frac{1}{2}(-n^1 h_x - n^2 h_y + n^3)^2 - \frac{g}{\epsilon}\right)\left[h_{xx}\left(1 + h_y^2\right) + h_{yy}\left(1 + h_x^2\right) - 2h_x h_y h_{xy}\right] \\ &+ g\left[(n^1 + h_x n^3)\left[\left(1 + h_y^2\right)\left(- h_x n^1_x - h_y n^2_x + n^3_x\right) - h_x h_y\left(- h_x n^1_y - h_y n^2_y + n^3_y\right)\right]\right. \\ &+ (n^2 + h_y n^3)\left.\left[\left(1 + h_x^2\right)\left(- h_x n^1_y - h_y n^2_y + n^3_y\right) - h_x h_y\left(- h_x n^1_x - h_y n^2_x + n^3_x\right)\right]\right] \\ &+ g(-n^1 h_x - n^2 h_y + n^3)\left[\left[\left(1 + h_y^2\right)\left(n^1_x + h_x n^3_x\right) - h_x h_y\left(n^1_y - h_x n^3_y\right)\right] + \left[\left(1 + h_x^2\right)\left(n^2_y + h_y n^3_y\right) - h_x h_y\left(n^2_x - h_y n^3_x\right)\right]\right] \end{aligned}$$

$$
\begin{aligned}
&+(n^1+n^3h_x)\bigg\{n^1\bigg[\big(1+h_y^2\big)\bigg(-h_{xx}g+\frac{1}{2}h_xg_x\bigg)-h_xh_y\bigg(-h_{xy}g+\frac{1}{2}h_xg_y\bigg)\bigg]\\
&+n^2\bigg[\big(1+h_y^2\big)\bigg(-h_{xy}g+\frac{1}{2}h_yg_x\bigg)-h_xh_y\bigg(-h_{yy}g+\frac{1}{2}h_yg_y\bigg)\bigg]+n^3\bigg[\big(1+h_y^2\big)\bigg(-\frac{1}{2}g_x\bigg)-h_xh_y\bigg(-\frac{1}{2}g_y\bigg)\bigg]\bigg\}\\
&+(n^2+n^3h_y)\bigg\{n^1\bigg[-h_xh_y\bigg(-h_{xx}g+\frac{1}{2}h_xg_x\bigg)+\big(1+h_x^2\big)\bigg(-h_{xy}g+\frac{1}{2}h_xg_y\bigg)\bigg]\\
&+n^2\bigg[-h_xh_y\bigg(-h_{xy}g+\frac{1}{2}h_yg_x\bigg)+\big(1+h_x^2\big)\bigg(-h_{yy}g+\frac{1}{2}h_yg_y\bigg)\bigg]+n^3\bigg[-h_xh_y\bigg(-\frac{1}{2}g_x\bigg)+\big(1+h_x^2\big)\bigg(-\frac{1}{2}g_y\bigg)\bigg]\bigg\},
\end{aligned}
\tag{B13}
$$

where the determinant of the metric tensor $g=1+h_x^2+h_y^2$, $g_x=2h_xh_{xx}+2h_yh_{xy}$, and $g_y=2h_xh_{xy}+2h_yh_{yy}$. If we consider nanowrinkling solutions such that we neglect $h_{\text{exact}}=h+O(||\nabla_{(\sigma)}h||^2)$ (10^{-6} of the whole contribution), we also replace 0 by $-\eta\,\mathrm{sgn}(\epsilon)\dot{h}$, and then Eq. (B13) reduces to a special type of Monge-Ampère equation (B14):

$$
\begin{aligned}
-\eta\ \mathrm{sgn}(\epsilon)\frac{dh}{dt}=&\bigg(-\frac{1}{\epsilon}+\frac{1}{2}(n^3)^2-(n^1)^2-3n^1n^3h_x-n^2n^3h_y\bigg)h_{xx}+\bigg(-\frac{1}{\epsilon}+\frac{1}{2}(n^3)^2-(n^2)^2-n^1n^3h_x-3n^2n^3h_y\bigg)h_{yy}\\
&-2(n^1n^2+n^2n^3h_x+n^1n^3h_y)h_{xy}+(-2n^1n_x^1-n^2n_y^1+2n^3n_x^3-n^1n_y^2)h_x\\
&+\big(-n^1n_x^2-2n^2n_y^2+2n^3n_y^3-n^2n_x^1\big)h_y+n^1n_x^3+n^2n_y^3+n^3\big(n_x^1+n_y^2\big).
\end{aligned}
\tag{B14}
$$

If we further approximate Eq. (B14) with $h_{\text{exact}}=h+O(||\nabla_{(\sigma)}h||)$ and let $|\epsilon|\ll 1$, the steady state periodic solution to Eq. (B14) can be analytically obtained by spectral method. Denote a and b such that $ax\in[0,2\pi]$ and $by\in[0,2\pi]$. The dimensionless approximated equation to Eq. (B14) degenerates to

$$
h_{xx}+h_{yy}=\epsilon\big[n^1n_x^3+n^2n_y^3+n^3\big(n_x^1+n_y^2\big)\big]=\epsilon P,
\tag{B15}
$$

with series solution

$$
h(x,y)=\sum_{j,k}-\frac{\epsilon\hat{P}_{j,k}}{(ja)^2+(kb)^2}e^{i(ajx+bky)},
\tag{B16}
$$

where $\hat{P}_{j,k}$ are the coefficients of the Fourier series $P=\sum_{j,k}\hat{P}_{j,k}e^{i(ajx+bky)}$.

APPENDIX C: DECOMPOSITION OF DIRECTOR FIELD

In this section, we decompose the director field on the local basis $\{\mathbf{r}_{y^1},\mathbf{r}_{y^2},\mathbf{k}\}$ such that $\mathbf{n}=n_\parallel^\alpha\mathbf{r}_\alpha+n_\perp\mathbf{k}$ and

$$
\mathbf{nn}=n_\parallel^\alpha n_\parallel^\beta\mathbf{r}_\alpha\mathbf{r}_\beta+n_\perp n_\parallel^\beta\mathbf{k}\mathbf{r}_\beta+n_\parallel^\alpha n_\perp\mathbf{r}_\alpha\mathbf{k}+n_\perp^2\mathbf{kk}.
\tag{C1}
$$

Since $||\mathbf{k}||=1$, $\mathbf{r}_\alpha\perp\mathbf{k}$, the following identities hold:

$$
\mathbf{k}\mathbf{r}_\beta:\nabla_{(\sigma)}\mathbf{k}=\mathbf{r}_\alpha\mathbf{k}:\nabla_{(\sigma)}\mathbf{k}=\mathbf{kk}:\nabla_{(\sigma)}\mathbf{k}=0.
\tag{C2}
$$

Combined with the fact that $2H=\mathbf{B}:\mathbf{I}_{(\sigma)}=-\nabla_{(\sigma)}\mathbf{k}:\mathbf{I}_{(\sigma)}$, the rotation pressure [in Eq. (7)] can be rewritten as

$$
P_{\text{rotation}}=W\mathbf{B}:\big(\mathbf{n}_\parallel\mathbf{n}_\parallel-n_\perp^2\mathbf{I}_{(\sigma)}\big).
\tag{C3}
$$

The surface gradient of director $\mathbf{n}$ is decomposed by

$$
\nabla_{(\sigma)}\mathbf{n}=\mathbf{r}^\beta\nabla_{(\sigma)\beta}\mathbf{n}=\mathbf{r}^\beta\mathbf{r}_\alpha\mathfrak{D}_\beta\mathfrak{n}_\parallel^\alpha+(\mathbf{B}\cdot\mathbf{n}_\parallel)\mathbf{k}+\nabla_{(\sigma)}\mathfrak{n}_\perp\mathbf{k}-\mathfrak{n}_\perp\mathbf{B},
\tag{C4}
$$

where $\mathfrak{D}$ is the surface covariant derivative defined by

$$
\begin{aligned}
D_\beta n_\parallel^\alpha=&\nabla_{(\sigma)\beta}n_\parallel^\alpha+n_\parallel^\mu(\nabla_{(\sigma)\beta}\nabla_{(\sigma)\mu}x^i\\
&+\nabla_{(\sigma)\beta}x^j\nabla_{(\sigma)\mu}x^m\Gamma_{jm}^i)g^{\alpha\nu}\mathbf{e}_i\cdot\mathbf{e}_k\nabla_{(\sigma)\nu}x^k
\end{aligned}
\tag{C5}
$$

and $\Gamma_{jm}^i=\partial_j\mathbf{e}_m\cdot\mathbf{e}_i$ are the Christoffel symbols with $3^3=27$ components.

The first term in the director pressure is

$$
\begin{aligned}
\mathbf{kn}:\nabla_{(\sigma)}\mathbf{n}=&\,\mathbf{kn}:(\mathbf{r}^\beta\mathbf{r}_\alpha\mathfrak{D}_\beta\mathfrak{n}_\parallel^\alpha+(\mathbf{B}\cdot\mathbf{n}_\parallel)\mathbf{k}\\
&+\nabla_{(\sigma)}n_\perp\mathbf{k}-n_\perp\mathbf{B}) \qquad\qquad (\text{C6})\\
=&\,(\mathbf{n}\cdot\mathbf{r}^\beta)\underbrace{(\mathbf{k}\cdot\mathbf{r}_\alpha)}_{0}\mathfrak{D}_\beta\mathfrak{n}_\parallel^\alpha+\mathbf{n}\cdot(\mathbf{B}\cdot\mathbf{n}_\parallel)\\
&+\mathbf{n}\cdot\nabla_{(\sigma)}n_\perp-n_\perp\underbrace{\mathbf{kn}:(B^{\alpha\beta}\mathbf{r}_\alpha\mathbf{r}_\beta)}_{0} \qquad (\text{C7})\\
=&\,\underbrace{\mathbf{n}_\perp\mathbf{n}_\parallel:\mathbf{B}}_{0}+\mathbf{n}_\parallel\mathbf{n}_\parallel:\mathbf{B}+\underbrace{\mathbf{n}_\perp\cdot\nabla_{(\sigma)}n_\perp}_{0}\\
&+\mathbf{n}_\parallel\cdot\nabla_{(\sigma)}n_\perp \qquad\qquad (\text{C8})\\
=&\,\mathbf{n}_\parallel\mathbf{n}_\parallel:\mathbf{B}+\mathbf{n}_\parallel\cdot\nabla_{(\sigma)}n_\perp. \qquad\qquad (\text{C9})
\end{aligned}
$$

The trace of the surface gradient is decomposed by

$$
\mathrm{tr}(\nabla_{(\sigma)}\mathbf{n})=\mathfrak{D}_\alpha n^\alpha-n_\perp\mathrm{tr}(\mathbf{B})=\nabla_{(\sigma)}\cdot(\mathbf{I}_{(\sigma)}\cdot\mathbf{n})-2Hn_\perp.
\tag{C10}
$$

The second tensor contraction in director pressure is

$$
(\mathbf{n}\cdot\mathbf{k})\,\mathrm{tr}(\nabla_{(\sigma)}\mathbf{n})=n_\perp\nabla_{(\sigma)}\cdot\mathbf{n}_\parallel-2Hn_\perp^2.
\tag{C11}
$$

Therefore, the director pressure [in Eq. (7)] can be written as

$$
-P_{\text{director}}=W[\mathbf{kn}:\nabla_{(\sigma)}\mathbf{n}+(\mathbf{n}\cdot\mathbf{k})\,\mathrm{tr}(\nabla_{(\sigma)}\mathbf{n})]
\tag{C12}
$$

$$
\begin{aligned}
&= W(\mathbf{n}_\parallel\mathbf{n}_\parallel : \mathbf{B} + \mathbf{n}_\parallel \cdot \nabla_{(\sigma)} n_\perp) \\
&\quad + W(n_\perp \nabla_{(\sigma)} \cdot \mathbf{n}_\parallel - 2H n_\perp^2) \qquad \text{(C13)}\\
&= \underbrace{W\mathbf{B} : (\mathbf{n}_\parallel\mathbf{n}_\parallel - n_\perp^2 \mathbf{I}_{(\sigma)})}_{+P_{\text{rotation}}} \\
&\quad + \underbrace{W(\mathbf{n}_\parallel \cdot \nabla_{(\sigma)} n_\perp + n_\perp \nabla_{(\sigma)} \cdot \mathbf{n}_\parallel)}_{\text{effective director pressure } P_E}. \qquad \text{(C14)}
\end{aligned}
$$

Equation (C14) implies that the local decomposition of the director pressure naturally contains the rotation pressure. Therefore, when we calculate the addition $P_{\text{dilation}} + P_{\text{rotation}} + P_{\text{director}}$, only the dilation pressure and an effective director pressure P_E are left. Replacing Eq. (C14) in $p_c = \nabla_{(\sigma)} \cdot \boldsymbol{\xi}$ in a second order anchoring model gives

$$
-p_c = 2H\gamma - \epsilon\gamma_0 \nabla_{(\sigma)} \cdot (n_\perp \mathbf{n}_\parallel). \qquad \text{(C15)}
$$

We define a vector $\mathcal{N} = n_\perp \mathbf{n}_\parallel$ and $\mathcal{N}$ is a surface tangential vector field. The surface balance equation is given by integrating Eq. (C15) over any area Ω enclosed by a boundary $\partial\Omega$. Notice that the surface divergence term on the right hand side can be converted to the line integral as follows:

$$
\iint_\Omega (2H\gamma + p_c) dA = \epsilon\gamma_0 \oint_{\partial\Omega} \mathcal{N} \cdot \boldsymbol{\mu}\, ds, \qquad \text{(C16)}
$$

shedding light on the effective director pressure as an edge effect on a patch Ω.

---

[1] H. K. Bisoyi, T. J. Bunning, and Q. Li, Stimuli-driven control of the helical axis of self-organized soft helical superstructures, Adv. Mater. **30**, 1706512 (2018).

[2] A. Scarangella, V. Soldan, and M. Mitov, Biomimetic design of iridescent insect cuticles with tailored, self-organized cholesteric patterns, Nat. Commun. **11**, 4108 (2020).

[3] S. N. Fernandes, Y. Geng, S. Vignolini, B. J. Glover, A. C. Trindade, J. P. Canejo, P. L. Almeida, P. Brogueira, and M. H. Godinho, Structural color and iridescence in transparent sheared cellulosic films, Macromol. Chem. Phys. **214**, 25 (2013).

[4] B. Natarajan and J. W. Gilman, Bioinspired bouligand cellulose nanocrystal composites: A review of mechanical properties, Philos. Trans. R. Soc. A **376**, 20170050 (2018).

[5] J. P. Lagerwall, C. Schütz, M. Salajkova, J. Noh, J. H. Park, G. Scalia, and L. Bergström, Cellulose nanocrystal-based materials: from liquid crystal self-assembly and glass formation to multifunctional thin films, NPG Asia Mater. **6**, e80 (2014).

[6] L. Feng, Y. Zhang, J. Xi, Y. Zhu, N. Wang, F. Xia, and L. Jiang, Petal effect: a superhydrophobic state with high adhesive force, Langmuir **24**, 4114 (2008).

[7] M.-M. Giraud-Guille, L. Besseau, and R. Martin, Liquid crystalline assemblies of collagen in bone and in vitro systems, J. Biomech. **36**, 1571 (2003).

[8] A. D. Rey and E. E. Herrera-Valencia, Liquid crystal models of biological materials and silk spinning, Biopolymers **97**, 374 (2012).

[9] M. Mitov, Cholesteric liquid crystals in living matter, Soft Matter **13**, 4176 (2017).

[10] B. D. Wilts, H. M. Whitney, B. J. Glover, U. Steiner, and S. Vignolini, Natural helicoidal structures: Morphology, self-assembly and optical properties, Mater. Today: Proc. **1**, 177 (2014).

[11] Y. Bouligand, Twisted fibrous arrangements in biological materials and cholesteric mesophases, Tissue Cell **4**, 189 (1972).

[12] Y. Bouligand, Liquid crystals and biological morphogenesis: Ancient and new questions, C. R. Chim. **11**, 281 (2008).

[13] M.-M. Giraud-Guille, Twisted plywood architecture of collagen fibrils in human compact bone osteons, Calcif. Tissue Int. **42**, 167 (1988).

[14] V. Sharma, M. Crne, J. O. Park, and M. Srinivasarao, Bouligand structures underlie circularly polarized iridescence of scarab beetles: A closer view, Mater. Today: Proc. **1**, 161 (2014).

[15] N. Guarín-Zapata, J. Gomez, N. Yaraghi, D. Kisailus, and P. D. Zavattieri, Shear wave filtering in naturally-occurring Bouligand structures, Acta Biomater. **23**, 11 (2015).

[16] R. Meister, H. Dumoulin, M.-A. Hallé, and P. Pieranski, The anchoring of a cholesteric liquid crystal at the free surface, J. Phys. II **6**, 827 (1996).

[17] V. V. Yuzhakov, P. V. Takhistov, A. E. Miller, and H.-C. Chang, Pattern selection during electropolishing due to double-layer effects, Chaos **9**, 62 (1999).

[18] Y. Shukla and M. Sharma, 'Egg-carton' shaped plausible organo-sedimentary structures from the Archaean Dharwar Craton, India, Int. J. Earth Sci. **109**, 931 (2020).

[19] A. Ludu, *Nonlinear Waves and Solitons on Contours and Closed Surfaces* (Springer Science & Business Media, New York, 2012).

[20] S. Schauer, M. Worgull, and H. Hölscher, Bio-inspired hierarchical micro- and nano-wrinkles obtained via mechanically directed self-assembly on shape-memory polymers, Soft Matter **13**, 4328 (2017).

[21] H. W. Meyer, W. Richter, and G. Brezesinski, Convex-concave curvatures in bilayers of dipalmitoylphosphatidylcholine and cholesterol induced by amphotericin B/deoxycholate after prolonged storage, Biochim. Biophys. Acta (BBA)-Biomembranes **1190**, 9 (1994).

[22] N. A. Yaraghi, N. Guarín-Zapata, L. K. Grunenfelder, E. Hintsala, S. Bhowmick, J. M. Hiller, M. Betts, E. L. Principe, J.-Y. Jung, L. Sheppard *et al.*, A sinusoidally architected helicoidal biocomposite, Adv. Mater. **28**, 6835 (2016).

[23] O. Scho, R. C. Desai *et al.*, Phase-ordering kinetics on curved surfaces, Physica A **239**, 412 (1997).

[24] A. D. Rey, Capillary models for liquid crystal fibers, membranes, films, and drops, Soft Matter **3**, 1349 (2007).

[25] A. D. Rey, Thermodynamics of soft anisotropic interfaces, J. Chem. Phys. **120**, 2010 (2004).

[26] A.-G. Cheong and A. D. Rey, Cahn-Hoffman capillarity vector thermodynamics for liquid crystal interfaces, Phys. Rev. E **66**, 021704 (2002).

[27] A. D. Rey, Interfacial thermodynamics of polymeric mesophases, Macromol. Theory Simul. **13**, 686 (2004).

[28] G. Gupta, D. K. Hwang, and A. D. Rey, Optical and structural modeling of disclination lattices in carbonaceous mesophases, J. Chem. Phys. **122**, 034902 (2005).

[29] A. D. Rey, Flow and texture modeling of liquid crystaline materials, Rheol. Rev. **6**, 71 (2009).

[30] A. D. Rey, Generalized Young-Laplace equation for nematic liquid crystal interfaces and its application to free-surface defects, Mol. Cryst. Liq. Cryst. Sci. Technol., Sect. A **369**, 63 (2001).

[31] S. K. Das and A. D. Rey, Texture formation under phase ordering and phase separation in polymer-liquid crystal mixtures, J. Chem. Phys. **121**, 9733 (2004).

[32] S. K. Das and A. D. Rey, Colloidal crystal formation via polymer–liquid-crystal demixing, Europhys. Lett. **70**, 621 (2005).

[33] G. De Luca and A. Rey, Monodomain and polydomain helicoids in chiral liquid-crystalline phases and their biological analogues, Eur. Phys. J. E **12**, 291 (2003).

[34] A. D. Rey, Liquid crystal models of biological materials and processes, Soft Matter **6**, 3402 (2010).

[35] M. Yada, J. Yamamoto, and H. Yokoyama, Spontaneous formation of regular defect array in water-in-cholesteric liquid crystal emulsions, Langmuir **18**, 7436 (2002).

[36] M. Yada, J. Yamamoto, and H. Yokoyama, Generation mechanism of shear yield stress for regular defect arrays in water-in-cholesteric liquid crystal emulsions, Langmuir **19**, 3650 (2003).

[37] A. D. Rey and M. M. Denn, Dynamical phenomena in liquid-crystalline materials, Annu. Rev. Fluid Mech. **34**, 233 (2002).

[38] A. D. Rey, E. E. Herrera-Valencia, and O. F. Aguilar Gutierrez, Liquid crystalline polymers: Structure and dynamics, in *Liquid Crystalline Polymers* (Springer Nature Switzerland AG, Cham, 2020).

[39] A. D. Rey, Simple shear and small amplitude oscillatory rectilinear shear permeation flows of cholesteric liquid crystals, J. Rheol. **46**, 225 (2002).

[40] A. D. Rey, Generalized cholesteric permeation flows, Phys. Rev. E **65**, 022701 (2002).

[41] P. Rofouie, Z. Wang, and A. Rey, Two-wavelength wrinkling patterns in helicoidal plywood surfaces: Imprinting energy landscapes onto geometric landscapes, Soft Matter **14**, 5180 (2018).

[42] Z. Wang, P. Rofouie, and A. D. Rey, Surface anchoring effects on the formation of two-wavelength surface patterns in chiral liquid crystals, Crystals **9**, 190 (2019).

[43] Z. Wang, P. Servio, and A. D. Rey, Mechanogeometry of nanowrinkling in cholesteric liquid crystal surfaces, Phys. Rev. E **101**, 062705 (2020).

[44] R. Goetz and W. Helfrich, The egg carton: Theory of a periodic superstructure of some lipid membranes, J. Phys. II **6**, 215 (1996).

[45] G. Brown and A. Chakrabarti, Ordering of block copolymer melts in confined geometry, J. Chem. Phys. **102**, 1440 (1995).

[46] Z. Wang, P. Servio, and A. Rey, Biaxial nanowrinkling in cholesteric surfaces: Egg carton surfaces through chiral anchoring, Colloid Interface Sci. Commun. **41**, 100372 (2021).

[47] D. Liu, C. W. Bastiaansen, J. M. den Toonder, and D. J. Broer, Photo-switchable surface topologies in chiral nematic coatings, Angew. Chem., Int. Ed. **51**, 892 (2012).

[48] B. Terris, R. Twieg, C. Nguyen, G. Sigaud, and H. Nguyen, Force microscopy of chiral liquid-crystal surfaces, Europhys. Lett. **19**, 85 (1992).

[49] J. E. Kirkwood and G. G. Fuller, Liquid crystalline collagen: a self-assembled morphology for the orientation of mammalian cells, Langmuir **25**, 3200 (2009).

[50] A. A. Sonin, *The Surface Physics of Liquid Crystals* (Taylor & Francis, London, 1995).

[51] I. W. Stewart, *The Static and Dynamic Continuum Theory of Liquid Crystals: A Mathematical Introduction* (CRC Press, Boca Raton, FL, 2019).

[52] E. G. Virga, *Variational Theories for Liquid Crystals* (Chapman and Hall/CRC, London, 2018).

[53] J. C. Slattery, L. Sagis, and E.-S. Oh, *Interfacial Transport Phenomena* (Springer Science & Business Media, New York, 2007).

[54] Z. Wang, P. Servio, and A. D. Rey, Rate of entropy production in evolving interfaces and membranes under astigmatic kinematics: Shape evolution in geometric-dissipation landscapes, Entropy **22**, 909 (2020).

[55] J. Cahn and D. Hoffman, A vector thermodynamics for anisotropic surfaces—II. Curved and faceted surfaces, Acta Metall. **22**, 1205 (1974).

[56] D. W. Hoffman and J. W. Cahn, A vector thermodynamics for anisotropic surfaces: I. Fundamentals and application to plane surface junctions, Surf. Sci. **31**, 368 (1972).

[57] J. E. Taylor, II—Mean curvature and weighted mean curvature, Acta Metall. Mater. **40**, 1475 (1992).

[58] P. Rofouie, D. Pasini, and A. D. Rey, Nanostructured free surfaces in plant-based plywoods driven by chiral capillarity, Colloids Interface Sci. Commun. **1**, 23 (2014).

[59] W. Jiang and Q. Zhao, Sharp-interface approach for simulating solid-state dewetting in two dimensions: A Cahn–Hoffman ξ-vector formulation, Physica D **390**, 69 (2019).

[60] W. Jiang, Q. Zhao, and W. Bao, Sharp-interface model for simulating solid-state dewetting in three dimensions, SIAM J. Appl. Math. **80**, 1654 (2020).

[61] T. Han, Y. Han *et al.*, Solving large scale nonlinear equations by a new ODE numerical integration method, Appl. Math. **1**, 222 (2010).

[62] C. T. Kelley and D. E. Keyes, Convergence analysis of pseudo-transient continuation, SIAM J. Numer. Anal. **35**, 508 (1998).

[63] C. Kelley and L. Liao, Explicit pseudo-transient continuation, Computing **15**, 18 (2013).